European Journal of Medicinal Chemistry 253 (2023) 115339

Contents lists available at ScienceDirect

European Journal of Medicinal Chemistry

journal homepage: www.elsevier.com/locate/ejmech

Research paper

Exploring the anticancer activity and the mechanism of action of pyrrolomycins F obtained by microwave-assisted total synthesis

Marilia Barreca [a,1], Miriam Buttacavoli [b,1], Gianluca Di Cara [b], Cesare D'Amico [b], Emanuela Peri [b], Virginia Spanò [a], Giovanna Li Petri [a,c], Paola Barraja [a], Maria Valeria Raimondi [a,*], Patrizia Cancemi [b,**], Alessandra Montalbano [a]

[a] Department of Biological, Chemical and Pharmaceutical Sciences and Technologies (STEBICEF), University of Palermo, Via Archirafi 32, 90123, Palermo, Italy
[b] Department of Biological, Chemical and Pharmaceutical Sciences and Technologies (STEBICEF), University of Palermo, Viale delle Scienze, Building 16, 90128, Palermo, Italy
[c] Drug Discovery Unit, Ri.MED Foundation, Via Bandiera 11, 90133, Palermo, Italy

ARTICLE INFO

Keywords:
Pyrrolomycin
Anticancer activity
Microwave-assisted organic synthesis (MAOS)
Vacuoles
Tunneling nanotubes (TNTs)
Filopodia

ABSTRACT

Pyrrolomycins (PMs) are a family of naturally occurring antibiotic agents, isolated from the fermentation broth of *Actinosporangium* and *Streptomyces species*. Pursuing our studies on pyrrolomycins, we performed the total synthesis of the F-series pyrrolomycins (**1–4**) by microwave-assisted synthesis (MAOS), thus obtaining the title compounds in excellent yields (63–69%). Considering that there is no evidence so far of the anticancer effect of this class of compounds, we investigated PMs for their antiproliferative activity against HCT116 and MCF-7 cancer cell lines. PMs showed anticancer activity at submicromolar level with a minimal effect on normal epithelial cell line (hTERT RPE-1), and they were able to induce several morphological changes including elongated cells, cytoplasm vacuolization, long and thin filopodia as well as the appearance of tunneling nanotubes (TNTs). These data suggest that PMs could act by impairing the cell membranes and the cytoskeleton organization, with subsequent increase of ROS generation and the activation of different forms of non-apoptotic cell death.

1. Introduction

Natural products represent a valuable source for the development of highly specific bioactive molecules. Based on their wide chemical diversity, natural products are able to interact with biological macromolecules, thus exerting specific biochemical and pharmacological properties. As a matter of fact, several antibiotics and anticancer drugs developed so far derive from natural products [1].

In recent years, much attention has been paid to pyrrolomycins (PMs), a class of polyhalogenated antibiotics isolated from the fermentation broth of *Actinosporangium* and *Streptomyces* species (Fig. 1). PMs are small molecules characterized by a pyrrole nucleus and a phenyl ring linked by a one-carbon spacer. Decoration with electron-withdrawing atoms such as halogens or nitro groups in both aromatic rings increase, by an inductive-mesomeric effect, the acidity of the phenolic OH and pyrrole NH which may play a key role in their biological activity. Coherently, among the natural pyrrolomycin analogues reported in the literature, the pentachlorinated pyrrolomycin D has been shown to be the most potent. Furthermore, *Staphylococcus aureus* and *Streptococcus pneumoniae* are less sensitive to pyrrolomycin C, and more than 10-fold less susceptible to pyrrolomycins I and J, bearing a methoxy group on the phenyl ring [5].

In bacteria, PMs act mainly by interacting with biological membranes. Indeed, it was suggested that in the Gram-positive strain *S. aureus* [2–4], PMs interfere with the activity of Sortase A. Some PMs were shown to be powerful depolarizing membrane agents capable of specifically disturbing the proton gradient and decoupling oxidative phosphorylation by protonophoric action [5], coupled with the steric hindrance and narcotic effect derived from their enhanced lipophilicity in the context of cellular membranes [6].

* Corresponding author.
** Corresponding author.
E-mail addresses: mariavaleria.raimondi@unipa.it (M.V. Raimondi), patrizia.cancemi@unipa.it (P. Cancemi).
[1] These authors contributed equally to this work.

https://doi.org/10.1016/j.ejmech.2023.115339
Received 1 February 2023; Received in revised form 29 March 2023; Accepted 2 April 2023
Available online 5 April 2023

Considering that antiproliferative activity of PMs has been poorly explored and that marinopyrrolomycins have been reported to inhibit the growth of neuroblastoma cells at nanomolar concentrations [7], with the aim of further exploring the biological potential of pyrrolomycins, we have recently extended the field of investigation to evaluate the anticancer activity of this class of compounds [6]. From our study emerged that selected pyrrolomycins **5**, **5a-d,** and **C** (Fig. 2) showed an interesting antiproliferative at low micromolar level against colon (HCT116) and breast (MCF-7) cancer cell lines, while being less toxic to normal epithelial cells (hTERT RPE-1) [6].

These interesting results, supported by our experience in the synthesis of small molecules as bioactive compounds [8–15], prompted us to further investigate the antitumor potential of PMs for a better insight, considering also that new nitro- and polyhalogenated PMs (**5**, **5a-d**) as well as the two natural pyrrolomycins, **C** and $\mathbf{F_{2a}}$ (**2**) (used as reference compounds in microbiological assays) have been synthesized using the MAOS (microwave-assisted organic synthesis) technique [2,6]. In particular, we focused our attention on F-series PMs, which were obtained, in 1983, in very low yields (1–5%) through a complicated biosynthetic approach involving pH-controlled extractions and difficult purification processes [16,17]. By applying MAOS technique to the total synthesis of F-series PMs, for the first time to the best of our knowledge, we were able to isolate natural pyrrolomycins $\mathbf{F_1}$ (**1**), $\mathbf{F_{2a}}$ (**2**), $\mathbf{F_{2b}}$ (**3**), and $\mathbf{F_3}$ (**4**) in much higher yields (>63%) (Fig. 1), short reaction time, reducing processing costs, solid and solvent waste at the same time, thus ensuring greater adherence to the ecological standards currently requested also in the pharmaceutical industry.

All the synthesized F-series PMs were screened for their antiproliferative activity and their mechanism of action was explored, focusing on a possible link between impaired cell membranes, rearrangements of the cytoskeleton, induction of oxidative stress and subsequent activation of non-apoptotic cell death (autophagy and methuosis) which was observed in PMs treated cells. This study, for the first time, highlighted possible molecular mechanisms involved in PMs toxicity, with new features which require further investigations.

2. Results and discussion

2.1. Synthesis of F-series PMs

F-series PMs were obtained applying a MAOS strategy previously developed by us for the synthesis of **2** [2]. The key intermediate **7** was obtained through Grignard reaction between (1-pyrrolyl)magnesium bromide and 5-bromo-2-methoxybenzoyl chloride (Scheme 1). The subsequent halogenation reactions were carried out with the proper halogenating agent equivalent at a time (N-bromosuccinimide, NBS, or N-chlorosuccinimide, NCS) to reduce the formation of reaction by-products as in the case of a conventional synthetic approach. Indeed, since the halogenation reaction is not selective, it gives rise to complex reaction mixtures from which the isolation of the desired compounds is not easily accessible. On the contrary, by microwave irradiation (four cycles of 15 min each, 60 W, 90 °C) of **7** with three equivalents of NBS in acetonitrile as solvent, 5-bromo-2-methoxyphenyl-(3,4,5-tribromo-1*H*-pyrrol-2-yl)methanone **8**, was obtained as the only reaction product (89.2% yield) (Scheme 1, Table 1).

A three steps synthetic sequence allowed the isolation of 3,4-dibromo-5-chloro derivative **11** (R^1 = Cl, R^2 = R^3 = Br), from derivative **7**. It was initially brominated with an equimolar amount of NBS at position 4 (R^2) of the pyrrole ring, according to the order of reactivity influenced by the resonance forms of 2-acylpyrroles [2], thus leading to the monobromo derivative **9** (R^2 = Cl) which was isolated by crystallization from ethanol with a 78.6% yield. Further halogenation with a stoichiometric amount of NCS resulted in compound **10** (R^1 = Cl) as the only reaction product (91.0% yield). The final halogenation at C-3 required more microwave reaction cycles, probably as a consequence of the lower reactivity of this position towards aromatic electrophilic substitution reactions in 2-acylpyrroles. Thus, the microwave heating was carried out at 90 °C with a power of 60 W for four cycles of 15 min each, allowing the isolation of compound **11** as the only reaction product with a 88.3% yield (Scheme 1, Table 1).

Finally, 3-bromo-4,5-dichloro-1*H*-pyrrol-2-yl-(5-bromo-2-methoxyphenyl)methanone **13** was obtained from intermediate **7** through two consecutive halogenation reactions. The introduction of chlorine atoms at four (R^2) and five (R^1) positions on the pyrrole ring, was initially performed under MW irradiation with two equivalents of NCS thus achieving compound **12** (R^1 = R^2 = Cl, 73.8%).

Subsequent bromination with an equimolar amount of NBS, in acetonitrile as a solvent, by microwave heating (cycles of 15 min each, 60 W, 90 °C) delivered compound **13** as the only reaction product (89.1%) (Scheme 1, Table 1).

As a final reaction step, compounds **8**, **11,** and **13** underwent *O*-demethylation with an excess of aluminum chloride, in anhydrous dichloromethane as a solvent, at room temperature for 12 h. Finally, PMs **1**, **3,** and **4** were obtained after quenching the reaction with a 5% H_2SO_4 solution and subsequent crystallization from dichloromethane (63.1%, 68.7%, 66.9%, respectively yields) (Scheme 1, Table 1).

Analytical and spectroscopic measurements were carried out to confirm the structures of all molecules. Interestingly, when compound **7** was reacted with 1 M equivalent of NBS, the aromatic signal of 3-proton in the pyrrole nucleus showed an unusual chemical shift. Indeed,

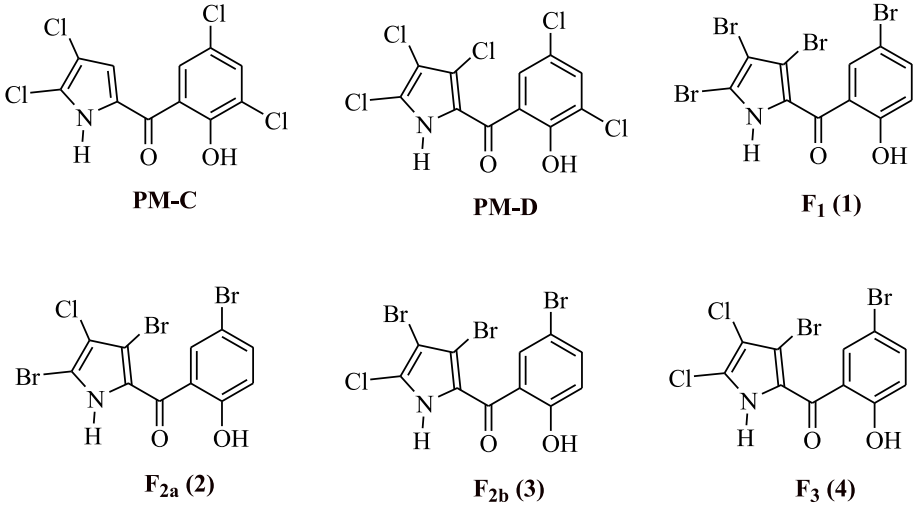

Fig. 1. Chemical structures of selected natural pyrrolomycins.

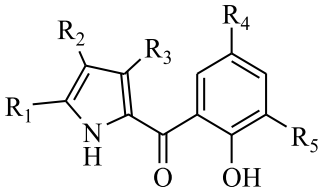

Pyrrolomycin	R^1	R^2	R^3	R^4	R^5
5	Br	Br	Br	Br	Br
5a	H	NO_2	H	Cl	Cl
5b	NO_2	Cl	H	Cl	Cl
5c	NO_2	Br	H	Cl	Cl
5d	Cl	Cl	NO_2	Cl	Cl
C	Cl	Cl	H	Cl	Cl

Fig. 2. Chemical structures of nitro- and polyhalogenated pyrrolomycins previously synthesized.

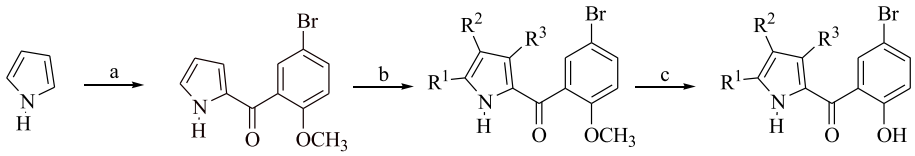

Scheme 1. *Reagents and reaction conditions:* (a) EthylMgBr, N_2, 0 °C; then, 5-bromo-2-methoxybenzoyl chloride, reflux, 30 min; then, r.t., 10% H_2SO_4, solution. 1 h; (b) NBS or NCS, MW heating: 90 °C, 60 W; (c) $AlCl_3$, r.t.,12 h then 5% H_2SO_4 solution.

Table 1
Pyrrolomycins **1**,**3**,**4** and (2-methoxyphenyl-1*H*-pyrrol-2-yl)methanones **8-13**

Compound	R^1	R^2	R^3
1	Br	Br	Br
3	Cl	Br	Br
4	Cl	Cl	Br
8	Br	Br	Br
9	H	Br	H
10	Cl	Br	H
11	Cl	Br	Br
12	Cl	Cl	H
13	Cl	Cl	Br

compound **9** showed two doublets at 7.15 and 8.24 δ for H-3 and for H-5, respectively. The 3-proton appeared more shielded than the expected by 2-carbonylpyrrole, probably due to the anisotropic effect of the phenyl ring, twisted with respect to the pyrrole ring. As reported in the literature, the introduction of a halogen into pyrrole rings caused only minor shifts in the resonance frequencies of the remaining hydrogen atoms [18].

Finally, for PMs **1**, **3** and **4**, were fully characterized and their structures confirmed by spectroscopic data.

2.2. Assessment of anticancer activity of F-series PMs

The synthesized F-series PMs (**1–4**) were screened to assess their anticancer activity against colon (HCT116) and breast cancer (MCF-7) cell lines, by using the MTT assay, comparing their cytotoxicity to our previous lead compound **5**, the pentabromide analogue. The non-tumoral epithelial cell line (hTERT-RPE-1) was also tested to evaluate the selectivity of selected PMs.

The cytotoxic activity (IC_{50} values) was estimated from a dose-response model, obtained by fitting sigmoidal curves of the cell percentage inhibition *versus* the logarithmic concentration of treatments (Fig. 3A). In general, all the synthesized PMs exhibited cytotoxic activity against the tested cancer cell lines, in a dose-dependent manner (Fig. S1, Supporting information), being the HCT116 more sensible to treatments compared to MCF-7. Moreover, the cytotoxic effects were less prominent in the non-tumoral epithelial cell line (hTERT-RPE-1), where a complete inhibition of cell viability was not recorded, even at higher concentrations. Based on the IC_{50} values (Fig. 3B), the cytotoxic activities ranged from 0.35 ± 0.1 μM for **1** in HCT116 to 1.21 ± 0.3 μM for **4** in MCF-7. These values fully fall within the clinically acceptable concentration of 100 mg L^{-1} [19], suggesting their potential application for injection or oral administration. The structure-activity relationship (SAR) showed that **1** was the most active among the F-series PMs, also compared with PM **5**, suggesting that not only the substituents of the pyrrole but also those of the phenol ring are important for the biological activity of PMs. Indeed, the replacement of the bromine in R^5 of PM **5** with a hydrogen atom on the phenol ring increased the antiproliferative activity on tumour cells. In addition, the removal of a halogen improved the safety profile of F-series PMs, which were found to be less toxic on hTERT-RPE-1 cells.

When the cytotoxicity of **2** and **3**, featuring a chlorine substituent in R^2 and R^1 positions respectively, was considered, a slight reduction of the activity was detected compared to **1**.

The PM **4** featuring two chlorine substituents in R^2 and R^1 was less active than **1**. All the analysed F-series PMs showed a strong selectivity against cancer cells compared to normal cells (about 100 times more active in cancer cells than in healthy cells), and, importantly, the replacement of the bromine (**5**) with hydrogen in R^5 position (F-series PMs) maximized their selectivity (Fig. 4).

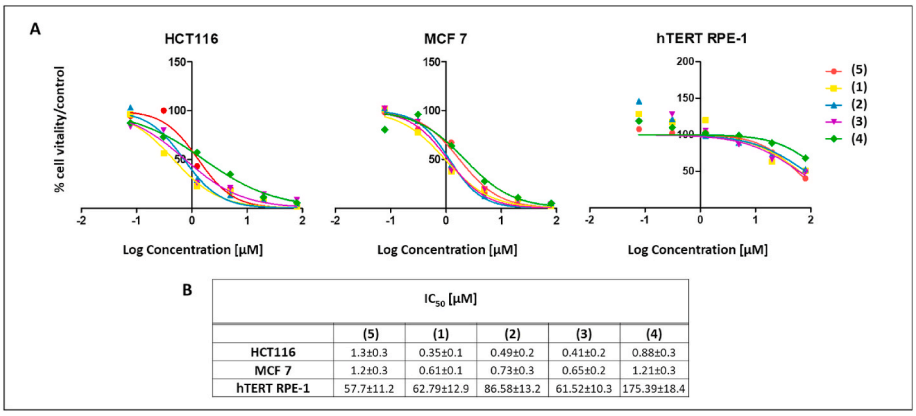

B

	IC_{50} [μM]				
	(5)	(1)	(2)	(3)	(4)
HCT116	1.3±0.3	0.35±0.1	0.49±0.2	0.41±0.2	0.88±0.3
MCF 7	1.2±0.3	0.61±0.1	0.73±0.3	0.65±0.2	1.21±0.3
hTERT RPE-1	57.7±11.2	62.79±12.9	86.58±13.2	61.52±10.3	175.39±18.4

Fig. 3. Cytotoxic curves of HCT116, MCF-7 cancer cells, and normal epithelial cell line hTERT-RPE-1 after challenge with increasing concentrations of selected PMs (**5, 1–4**) for 48 h (A); IC_{50} values (concentration that inhibit the 50% of cell proliferation compared to untreated cells) obtained from the dose-response model, expressed in μM ±SD (standard deviation) (B). Experiments were performed in triplicate.

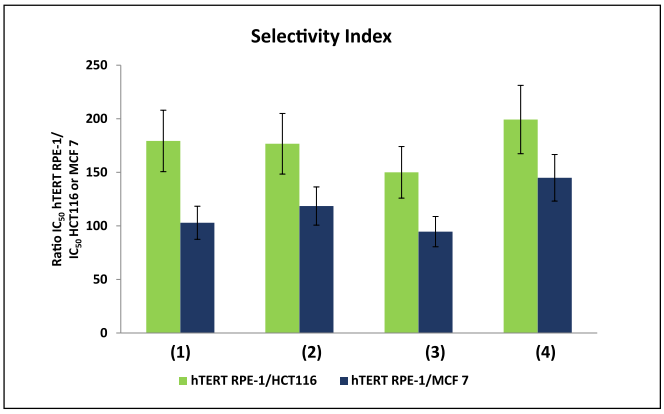

Fig. 4. Cancer Selectivity Index, defined as the ratio of IC_{50} of normal hTERT-RPE-1 to that of HCT116 and MCF-7 cancer cells, respectively for tested F-series PMs.

2.3. Assessment of morphological changes induced by F-series PMs treatment

Interestingly, information about the mechanism of action of PMs was derived from the morphological changes of treated cells. When cancer cells were incubated in the presence of 0.5 μM of selected PMs (Fig. 5, Fig. S2, Supporting information), a less clumped and more flattened morphology was detected under a phase-contrast microscope; filamentous protrusions began to appear, that had developed into long elongations or spikes at 48 h of treatment. These elongations, resembling filopodia are rich in actin (Fig. S3, Supporting information). Filopodia are multifunctional finger-like plasma membrane protrusions with bundles of actin filaments involved in a great range of cellular processes including micropinocytosis, autophagy as well as cell migration, wound healing, chemoattractant guidance, extracellular matrix adhesion and remodeling [20,21]. Specifically, during macropinocytosis, an actin-driven process, cells extend large membrane ruffles that fold back onto the cell surface and fuse to form pockets that pinch off from the plasma membrane, resulting in large intracellular vacuoles [22]. Filopodia biogenesis requires the local remodeling of cortical F-actin mediated by filament-severing proteins, such as cofilin [23], which we found upregulated in PMs-treated cells. Moreover, it was reported that lipid rafts (liquid-ordered plasma membrane microdomains) influence filopodia and lamellipodia formation [24], and dynamic membrane microdomains accumulate in the tips of filopodia [25], suggesting that, the dysregulation of membranes elements, such as phospholipid and cholesterol as well as cytoskeletal proteins impair cell polarity and cell morphology. Accordingly, we previously showed that the biological activity of PMs is due to the steric hindrance and narcotic effect derived from the lipophilicity of PMs in the context of cellular membranes [6].

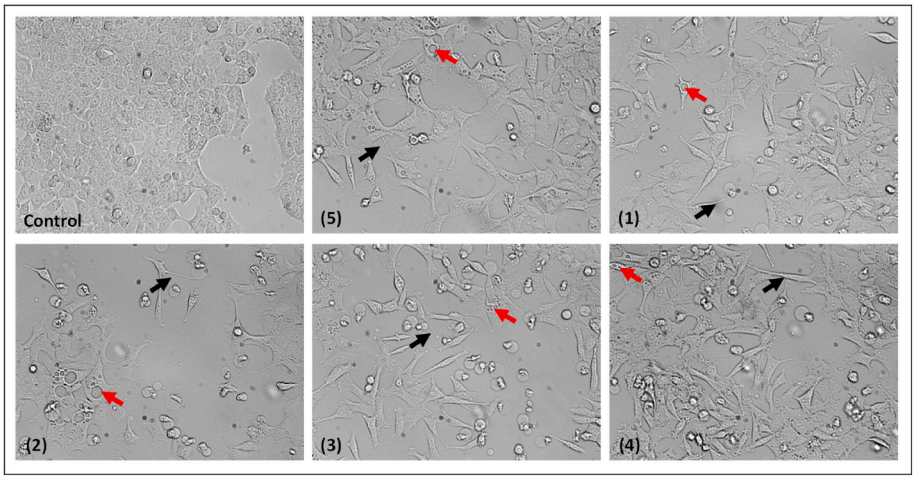

Fig. 5. Inverted phase-contrast micrographs of HCT116 cells treated for 48 h with 0.5 μM of selected PMs. Black arrows indicate cell projection, resembling filopodia. Red arrows indicate cell vacuoles. Magnification 200×.

Prominent vacuoles were also observed, whose number increased in a dose- and time-dependent manner. After 48 h of treatment, massive vacuolization was observed in several cells, and it might be due to the fusion of small vacuoles into ones (Fig. 5, red arrows).

It is well known that vacuole accumulation is an important initiating event, causing metabolic alterations or stress responses that lead to cell death, albeit indirectly [26]. Cytoplasmic vacuoles are formed from components of the endoplasmic reticulum or endosomal-lysosomal organelles [27]. ER vacuolization can be triggered by cellular osmotic stress and proceeds due to mitochondrial dysfunction and ATP pool depletion, which are causes of cell death. Vacuolization of endosomal-lysosomal components is instead related to disturbed sorting and/or fusion of the organelles or changed intraorganellar ionic balance, which leads to the dysfunction of macropinocytosis, endocytosis, and autophagy [28].

No morphological alteration was detected in hTERT-RPE-1 PMs-treated cells and, even at 5 μM of PMs-treatments for 48 h, in fact, treated cells displayed similar morphology to untreated ones (Fig. S4, Supporting information). Altogether, these alterations suggested that PMs biological activity could be due to the impairment of biological membranes together with cytoskeleton rearrangement.

To better analyse morphological abnormalities, Scanning Electron Microscopy (SEM) was performed after 48 h of HCT116-PMs treatment (Fig. 6A and B). Control cells showed a polygonal-shaped phenotype, with well-structured cell-cell adhesions, and mostly presented extracellular microvesicles (EVs) and microvilli on their surface. Significant changes in cell morphology, including flattened- and elongated-fusiform-shaped cells, neuronal sprouting, alteration of intercellular adhesion, massive vacuolization, leakage and perforation of the cell membranes, intensive membrane ruffling and blebbing, appearance of many long, thin filopodia were observed in treated cells.

Most cells appeared connected by straight and very thin bridge-like intercellular cytoplasmic processes, morphologically comparable to previously described tunneling nanotubes (TNTs), that enable long-range communication between connected cells [29]. Probably, the formation of TNTs occurs from filopodia [30] and containing actin microfilaments cross-linked into bundles by actin-bundling proteins and several transmembrane proteins.

The proposed functions of TNTs, still not well known, include the cell-to-cell transfer of vesicles, organelles [31], small molecules as well as electrical stimuli [32]. TNT-mediated electrical coupling can transfer depolarization from one cell to another or within organelles, resulting from the uncoupling of the transport as well as the oxidative phosphorylation of ATP in mitochondria. TNT formation and induction have been observed following different stresses, including oxidative stress [33,34]. Under these circumstances, cells may respond to the stresses or stimulations by activating signaling pathways that initiate cytoskeleton rearrangement, and promotion of TNTs formation. Besides the effects on the cytoskeleton, ROS can influence the properties of plasma membranes through the direct oxidation of phospholipids and cholesterol. Accordingly, a significant increase in oxidative stress upon PMs treatment was found. Based on these results, we suggest that oxidative stress may have an important impact on the biological activity of PMs, that in turn affect cell membranes, signalling pathways and cytoskeletal organization.

2.4. F-series PMs induce non-conventional cell death in HCT116 cells

To identify the cell death mechanism induced by PMs in the HCT116 cell line, the nuclei of treated cells were examined. Staining with

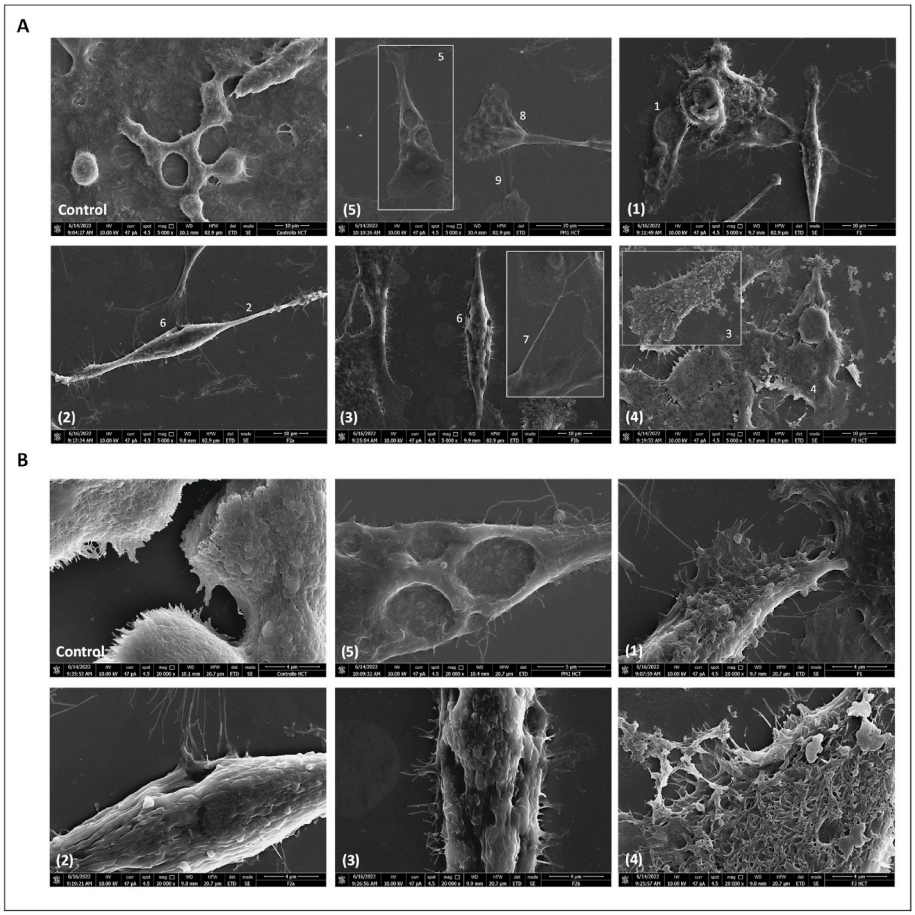

Fig. 6. Scanning electron microscopy (SEM) micrographs of HCT116 cells treated for 48 h with 0.5 μM of selected PMs. Untreated cells showed a polygonal-shaped phenotype and cells showed extracellular micro-vesicles (EVs) and microvilli on their surface. PMs-treated cells showed a plethora of morphological abnormalities, including flattened cells (1), elongated cells (2), intensive membrane ruffling and blebbing (3), alteration of intercellular adhesion (4), massive vacuolization (5), leakage and perforation of the cell membranes (6), neuronal-like sprouting (8) long and thin filopodia (9), and tunneling nanotubes (TNTs) (7). A) Magnification 5000×; B) Magnification 20000×.

Hoechst 33342 showed that the nuclei of treated cells (0.5 μM of PMs for 48 h), were still intact and no significant chromatin condensation or nuclear fragmentation was observed (Fig. 7). PMs-treated HCT116 cells were also stained with acridine orange and ethidium bromide (AO/EB). As shown in Fig. 8, untreated viable cells emitted green fluorescence due to the AO staining of both cytoplasm and nuclei. Several nuclei of PMs-treated cells exhibited orange fluorescence due to EB stain following a loss of membrane integrity; membrane blebbing, but not condensed chromatin was also detected. The AO staining in the cytoplasm of treated cells was detectable as bright punctate dots (both orange and red), revealing acidic compartments [35], such as lysosomes and vacuole, namely acidic vesicular organelles (AVOs). Moreover, some vacuoles originated from an engulfment of extracellular fluid with neutral pH were observed. Altogether, these features are not specific to apoptotic cell death but represent the hallmark of many non-apoptotic cell death mechanisms. Among the non-apoptotic cell death, autophagy is one of the well-known, characterized by autophagosomes (double-membrane vacuoles). In contrast, methuosis, a recently described non-apoptotic cell death, utilizes single-membrane vacuoles from macropinocytosis. A few other types of non-apoptotic cell death mechanisms share a similar origin for the formation of cytoplasmic vacuoles. Oncosis, paraptosis, and necroptosis form vacuoles from the endoplasmic reticulum (ER) and mitochondria [28,36–38]. Consistently, a distinct characteristic of many non-apoptotic cell death mechanisms is massive vacuolization.

The expression of different markers related to survival pathways (AKT1-2-3, Bcl-2), autophagic cell death (Atg-7, Beclin-1, LC3B-I/LC3B-II), epithelial to mesenchyme transition (E-cadherin and vimentin) and cytoskeletal proteins (Cofilin and Tubulin) were analysed by Western blotting (Fig. 9). Regarding the survival pathways, a slight decrease of AKT and a more variable expression of Bcl-2 were detected in PM-treated cells. Among the proteins involved in autophagic cell death, a significant upregulation of LC3-II especially in **3** and **4** treated cells and a concomitant downregulation of LC3B-I was detected. The expression of other autophagic markers, namely Atg-7 and Beclin-1, was more variable, and significantly upregulated in PM **5** treated cells. As expected, the expression of the E-cadherin, a specific marker of epithelial phenotype, and the Vimentin, a specific marker of mesenchymal phenotype remained unvaried in the PM-treated cells, suggesting that the morphological changes did not depend on epithelial to mesenchymal transition (EMT). Finally, while the expression of Cofilin, an actin-binding protein involved in the regulation of F-actin polymerization/depolymerization kinetics and filopodial structure [39,40] was upregulated, a slight downregulation of the tubulin was detected in PMs treated cells. It is worth noting that PM **5** treated cells often exhibited a different trend in protein expression compared to other PM treatments, suggesting that structural changes in PMs can influence the activation of specific pathways. Collectively, these data confirmed that PMs induce several supposed non-conventional cell deaths, and impair cytoskeleton organization.

2.5. *Effect of F-series PMs on intracellular oxygen species*

There is a growing body of evidence supporting the hypothesis that cell membrane impairment as well as the perturbation of cytoskeletal proteins represent one of the earliest targets of oxidative stress [41,42]. Moreover, the elevation of intracellular ROS (Reactive Oxygen Species) levels is known to induce oxidative stress and cell death [43,44].

Based on these concerns, the effect of PMs treatment on intracellular levels of ROS by dichlorodihydrofluorescein diacetate (DCFH-DA) was investigated. HCT116 cells were treated for 24 and 48 h with the IC_{50} of selected PMs. As shown in Fig. 10A, the exposure to PMs induced a remarkable ROS increase in a time-dependent manner, suggesting an important role of ROS in PMs toxicity. The increase of ROS was also confirmed by micrographs performed on fluorescence microscopy after 48 h of treatment (Fig. 10B).

3. Conclusions

Here, the total synthesis of F-series PMs by the MAOS technique and their anticancer properties were deeply investigated.

All the synthesized PMs showed a prominent cytotoxic activity against the tested cancer cell lines, being the **1** the most active pyrrolomycin. The cytotoxicity decreased from **1** to **2**, **3**, and **4**, whereas the selectivity was higher in **4** compared to the other PMs. Since **1** differ from **2** and **3** for the substitution of one bromine with chlorine, and **4** for the replacement of two bromine with chlorine, we surmise that the biological activity of PMs is influenced by the presence of bromine

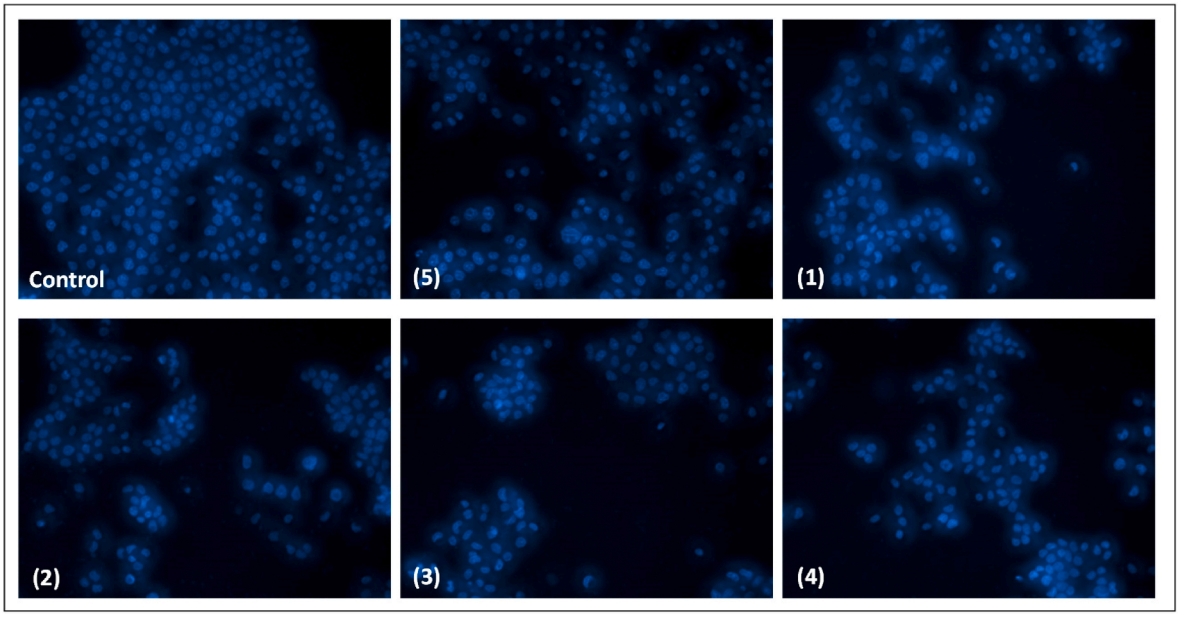

Fig. 7. Hoechst 33342 staining of HCT116 cells showed a uniform nuclear stain, both in HCT116 control cells and in PMs treated cells (0.5 μ M for 48 h). No significant number of cells with nuclear fragmentation and/or condensed chromatin, typical of the apoptotic cell was detected. As expected, a slight reduction in cell number was observed. Magnification 200×.

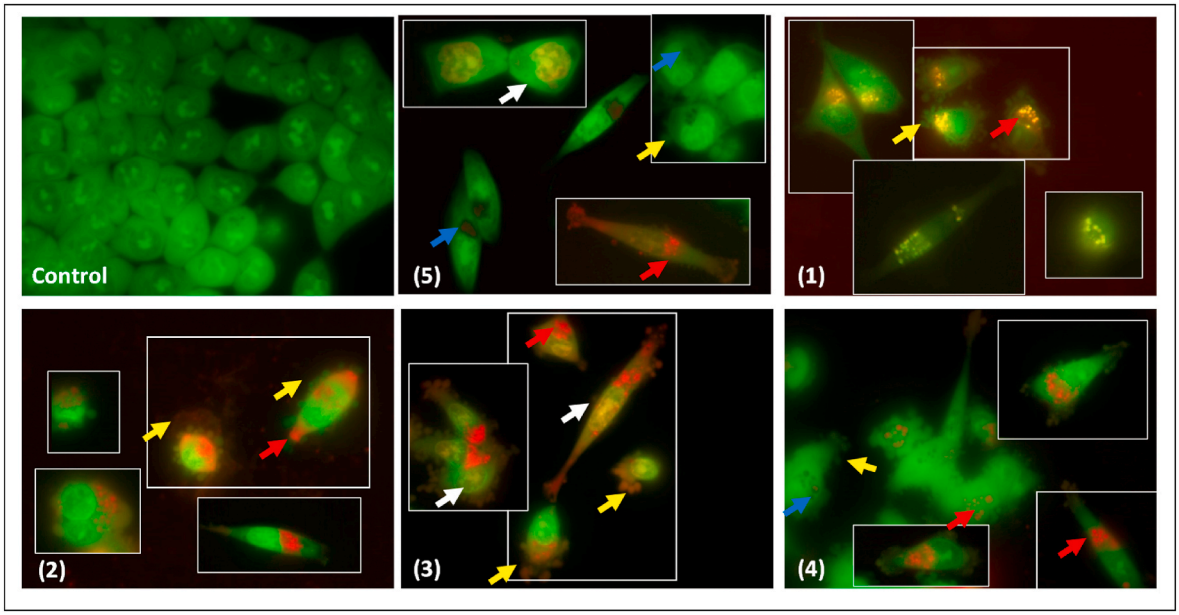

Fig. 8. Fluorescence micrographs of HCT116 cells treated 48 h with 0.5 μM of selected PMs after AO/EB double staining. Untreated viable cells display green fluorescence of both cytoplasm and nuclei. Several nuclei of PMs-treated cells exhibited orange fluorescence stain (blank arrows) following loss of membrane integrity and membrane blebbing (yellow arrows). In the cytoplasm are visible bright punctate dots, both orange and red, (red arrows), namely acidic vesicular organelles (AVOs). Some neutral-pH vacuoles (blue arrows) are also detected. Magnification 630×.

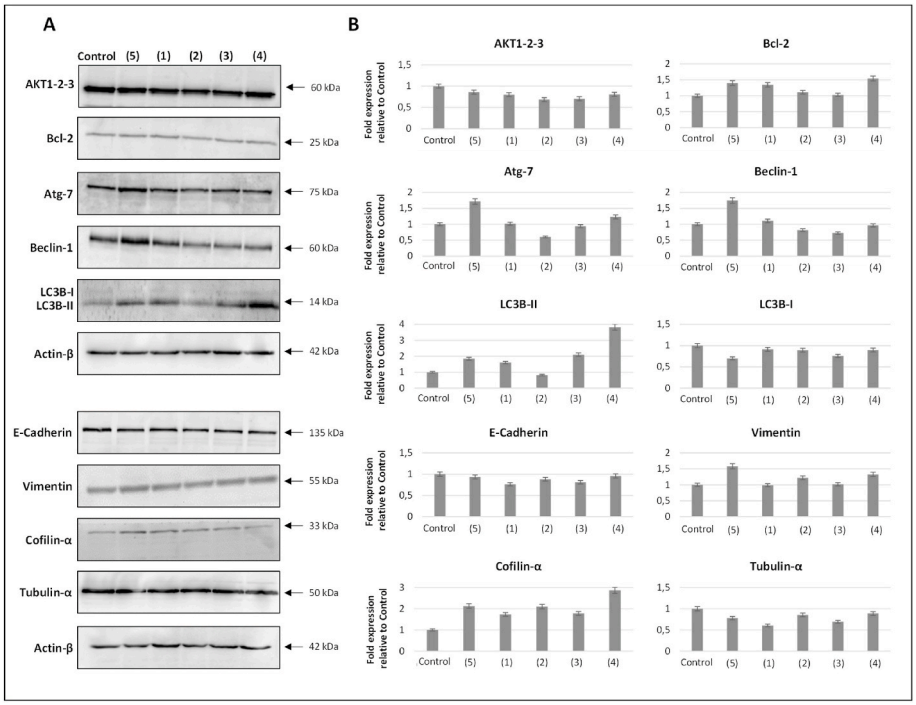

Fig. 9. Western blotting analysis showing the effect of PMs treatment (0.5 μM for 48 h) on the expression of AKT, Bcl-2, Atg-7, Beclin-1, LC3B-I/LC3B-II, E-cadherin, Vimentin, Cofilin, and Tubulin, in HCT116 cells. Actin-β was used as a loading control (A). Western blot quantification was normalized against the Actin-β signal and referred to the untreated control cells (B).

atoms. The reduced activity of **2** and **3** respect to **1** could be explained on the basis of their ability to permeate, mainly influenced by molecular size, ionic charge, and lipophilicity [45,46]; moreover, literature data indicate that brominated compounds induce blood cell lysis at concentrations 10-fold lower than chlorinated compounds [47] and have also shown 120-1200-fold more oxidising activity than chlorinated analogues [48].

The HCT116 cells treated with F-series PMs underwent severe morphologic changes, such as a less clumped and more flattened morphology and the appearance of filamentous protrusions or ruffles and spikes, resembling filopodia.

SEM analyses showed that most PMs-treated cells appeared connected by tunneling nanotubes (TNTs). TNT formation and induction have been observed following different stresses, including oxidative

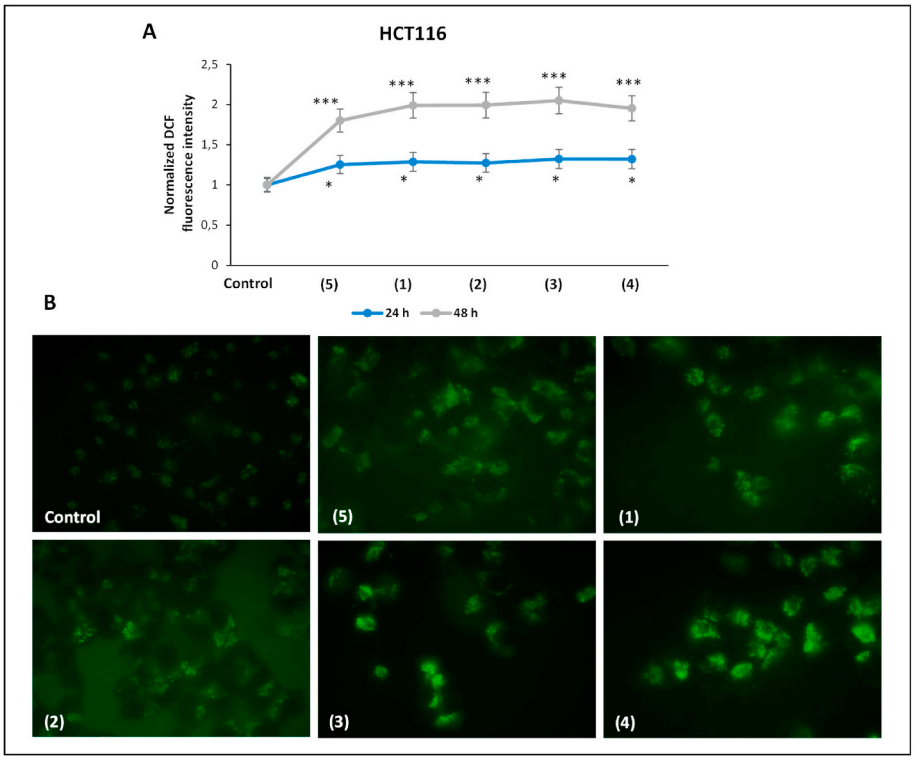

Fig. 10. Detection of intracellular ROS generation in PMs-treated cells (IC_{50} values for 24 and 48 h). ROS was measured using DCFH-DA and quantified through spectrofluorometry (A). Data were normalized for cell number determined by MTT assay and expressed with respect to the untreated cells used as control. Statistical significance was assessed by the Student's t-test: *$p < 0.05$ and ***$p < 0.001$. The data are expressed as mean value ± SD. (B) Fluorescence micrographs of 48 h-PMs treated cells after incubation with DCFH-DA. Magnification 640×.

stress [33,34]. Under these circumstances, cells may respond to the stresses or stimulations by activating signaling pathways that initiate cytoskeleton rearrangement, and promotion of TNTs formation. Besides the effects on the cytoskeleton, ROS can influence the properties of plasma membranes through the direct oxidation of phospholipids and cholesterol. Accordingly, a significant increase in oxidative stress upon PMs treatment was found. Based on these results, we suggest that oxidative stress may have an important impact on the biological activity of PMs, that in turn affect cell membranes, signalling pathways and cytoskeletal organization.

Regarding the cell death mechanisms, our results are consistent with the induction of autophagy, as suggested by the upregulation of acidic vesicular organelles (AOVs), the downregulation of AKT, and the increment of several autophagic markers, but also with the induction methuosis, as suggested by the absence of chromatin condensation or nuclear fragmentation. Thus, the identification of vacuole origin and properties will help elucidate the specific mechanism of PMs-induced cell death.

In conclusion, PMs can be considered as promising molecules not only for their biological activity but more importantly for their non-canonical mode of action on the cell membranes and cytoskeleton. Further efforts should be analysing the dynamics PMs activity to understand what are the causal and consequential events and the connectivity between activated pathways.

4. Experimental section

4.1. Chemistry section

4.1.1. Materials and instruments

Melting points were determined on a Stuart SMP30 melting point apparatus and are uncorrected. IR spectra were recorded at room temperature in KBr disks with a PerkinElmer Infrared 137 E spectrometer. ^{1}H NMR (400 MHz) and ^{13}C NMR (100 MHz) spectra were recorded with a Bruker AC-E spectrometer at room temperature in DMSO-d_6 or $CDCl_3$, unless otherwise specified, using tetramethylsilane as internal standard; chemical shifts (δ) are expressed as ppm values. Microwave reactions were performed with an Anton Paar GmbH - Monowave 300 (Microwave synthesis reactor). Medium Pressure Liquid Chromatography (MPLC) was performed with the CombiFlash RF200 (TeleDyne Isco) using prepacked silica gel column (0.040–0.063 mm). Microanalyses (C, H, N) were carried out with the Elemental Vario EL III apparatus and agreed with theoretical values ± 0.4%. The purity of all the tested compounds was >95%, determined by HPLC (Agilent 1100 series). All reactions were monitored by TLC on precoated aluminum sheets 20 × 20 (0.2 mm Kieselgel 60 G F254, Merck) and C-18 reverse phase (RP-18 F254, Merck) using UV light at 254 nm for visualization. All reagents and solvents were from Aldrich, Fluka, Merck, Across or J.T. Baker.

4.1.2. Methods

4.1.2.1. Preparation of (5-Bromo-2-methoxyphenyl)(1H-pyrrol-2-yl) methanone (7). A cold solution of freshly distilled pyrrole (20 mmol) in anhydrous diethyl ether (100 mL) was added, dropwise and under a nitrogen atmosphere, to a cold suspension of ethyl magnesium bromide (20 mmol) in anhydrous diethyl ether. Then, a solution of 5-bromo-2-methoxybenzoyl chloride (20 mmol) in anhydrous diethyl ether (100 mL) was slowly added at 0 °C. The resulting reaction mixture was refluxed for 30 min and, after cooling to room temperature, a 10% sulfuric acid solution (100 mL) was added. After 1 h of magnetic stirring, the ether was separated from the aqueous phase, then extracted with diethyl ether (2×100 mL). Finally, the combined organic extracts were washed with distilled water (2 × 50 mL), dried over anhydrous sodium sulfate and the solvent removed under reduced pressure. The (5-bromo-2-methoxyphenyl)(1*H*-pyrrol-2-yl)methanone **7** was purified by MLPC using an ethyl acetate/cyclohexane mixture (v/v 15/85) as eluent, and a 50 g prepacked silica gel column. White solid, yield 43.1%, mp 116–117 °C. IR (cm^{-1}): 1610 (CO); 3205 (NH). ^{1}H NMR ($CDCl_3$) δ: 3.80 (3H, s, CH_3), 6.27–6.29 (m, 1H, Ar), 6.65–6.67 (m, 1H, Ar), 6.87–6.90 (m, 1H, Ar), 7.15–7.17 (m, 1H, Ar), 7.51–7.54 (m, 2H, Ar), 10.31 (bs, 1H, NH). ^{13}C NMR: 56.6, 104.6, 112.3, 112.6, 114.7, 120.9, 127.9, 130.5, 131.1, 134.9, 156.6, 181.5.

Anal. calc. for $C_{12}H_{10}BrNO_2$: C, 51.45%; H, 3.60%; N, 5.00%. Found: C, 51.53%; H, 3.66%; N, 5.07%.

*4.1.2.2. General procedure for preparation of substituted (2-methoxyphenyl-1H-pyrrol-2-yl)methanones (**8**–**13**).* To a solution of compounds **7,9,10,12** (1 mmol) in acetonitrile as solvent (2 mL), freshly crystallized N-bromosuccinimide (NBS) or N-chlorosuccinimide (NCS) was added, and the reaction mixture was irradiated with a monomodal microwave reactor at 90 °C and power of 60W.

The reaction mixture was evaporated under reduced pressure and the residue was partitioned between water (10 mL) and diethyl ether (10 mL) and, subsequently, extracted twice with diethyl ether (10 mL). The combined extracts were washed with water, dried over anhydrous sodium sulfate and evaporated. The crude product was crystallized from ethanol to give pure compounds **8–13**.

*4.1.2.3. (5-Bromo-2-methoxyphenyl)(3,4,5-tribromo-1H-pyrrol-2-yl) methanone (**8**).* This compound was obtained from reaction of **7** with three equivalents of NBS by microwave heating for 4 cycles of 15 min each. White solid, Yield 89.2%, mp 188–189 °C. IR (cm^{-1}): 1609 (CO); 3211 (NH). ^{1}H NMR (DMSO-d_6) δ: 3.71 (s, 3H, CH_3), 7.09 (d, 1H, J = 8.9 Hz, H-3′), 7.39 (d, 1H, J = 2.5 Hz H-6′), 7.64 (dd, 1H, J = 8.9, 2.5 Hz, H-4'), 13.00 (bs, 1H, NH).^{13}C NMR (DMSO-d_6) δ: 56.5, 102.5, 105.9, 112.8, 112.9, 114.7, 125.4, 129.0, 131.3, 134.6, 158.1, 180.2.

Anal. calc. for $C_{12}H_7Br_4NO_2$: C, 27.89%; H, 1.37%; N, 2.71%. Found: C, 27.95%; H, 1.43%; N, 2.77%.

*4.1.2.4. (5-Bromo-2-methoxyphenyl)(4-bromo-1H-pyrrol-2-yl)methanone (**9**).* This compound was obtained from reaction of **7** with equimolar amount of NBS by microwave heating for 5 min at 90 °C, power of 60W. White solid, Yield 78.6%, mp 118–119 °C. IR (cm^{-1}): 1619 (CO); 3242 (NH). ^{1}H NMR (DMSO-d_6) δ: 3.90 (s, 3H, CH_3), 7.15 (d, 1H, J = 1.6 Hz, H-3), 7.40 (d, 1H, J = 9.3 Hz, H-3′), 8.24 (d, 1H, J = 1.6 Hz, H-5), 8.26 (d, 1H, J = 2.9 Hz H-6′), 8.42 (dd, 1H, J = 9.3, 2.9 Hz, H-4'), 13.31 (bs, 1H, NH).^{13}C NMR (DMSO-d_6) δ: 57.3, 94.5, 112.9, 113.3, 113.9, 125.1, 125.9, 127.0, 128.4, 129.5, 158.9, 180.7.

Anal. calc. for $C_{12}H_9Br_2NO_2$: C, 40.15%; H, 2.53%; N, 3.90%. Found: C, 40.23%; H, 2.61%; N, 4.01%.

*4.1.2.5. (4-Bromo-5-chloro-1H-pyrrol-2-yl)(5-bromo-2-methoxyphenyl) methanone (**10**).* This compound was obtained from reaction of **9** with equimolar amount of NCS by microwave heating for 5 min at 90 °C, power of 60W. White solid, Yield 91.0%, mp 139–140 °C. IR (cm^{-1}): 1612 (CO); 3200 (NH). ^{1}H NMR (DMSO-d_6) δ: 3.74 (s, 3H, CH_3), 7.00–7.04 (m, 1H, Ar), 7.14 (d, 1H, J = 8.0 Hz, Ar), 7.31 (dd, 1H, J = 7.5, 2.7 Hz Ar), 7.46–7.51 (m, 1H, Ar), 13.28 (bs, 1H, NH).

^{13}C NMR (DMSO-d_6) δ: 56.0, 104.2, 111.7, 112.5, 118.1, 118.6, 124.6, 129.2, 132.3, 147.2, 157.6, 180.4.

Anal. calc. for $C_{12}H_8Br_2ClNO_2$: C, 36.63%; H, 2.05%; N, 3.56%. Found: C, 36.69%; H, 2.10%; N, 3.63%.

*4.1.2.6. (5-Bromo-2-methoxyphenyl)(3,4-dibromo-5-chloro-1H-pyrrol-2-yl)methanone (**11**).* This compound was obtained from reaction of **10** with equimolar amount of NBS, microwave heating at 90 °C, power of 60W for 4 cycles of 15 min each. White solid, Yield 88.3%, mp 182–183 °C. IR (cm^{-1}): 1609 (CO); 3200 (NH). ^{1}H NMR (DMSO-d_6) δ: 3.73 (s, 3H, CH_3), 7.10 (d, 1H, J = 9.0 Hz, H-3′), 7.45 (d, 1H, J = 2.5 Hz, H-6′), 7.65 (dd, 1H, J = 9.0, 2.5 Hz H-4'), 13.54 (bs, 1H, NH). ^{13}C NMR (DMSO-d_6) δ: 56.6, 110.0, 110.6, 112.9, 114.7, 125.5, 131.1, 133.0, 134.8, 150.6, 158.2, 180.3.

Anal. calc. for $C_{12}H_7Br_3ClNO_2$: C, 30.51%; H, 1.49%; N, 2.97%. Found: C, 30.55%; H, 1.53%; N, 3.04%.

*4.1.2.7. (5-Bromo-2-methoxyphenyl)(4,5-dichloro-1H-pyrrol-2-yl)methanone (**12**).* This compound was obtained from reaction of **7** with two equivalents of NCS, microwave heating at 90 °C, power of 60W for 2 cycles of 5 min each. White solid, Yield 73.8%, mp 141–142 °C. IR (cm^{-1}): 1609 (CO); 3200 (NH). ^{1}H NMR (DMSO-d_6) δ: 3.73 (s, 3H, CH_3), 6.99–7.03 (m, 1H, Ar), 7.13 (d, 1H, J = 8.4 Hz, Ar), 7.31 (dd, 1H, J = 7.5, 1.7 Hz Ar), 7.46–7.50 (m, 1H, Ar), 13.29 (bs, 1H, NH).^{13}C NMR (DMSO-d_6) δ: 56.0, 111.7, 112.6, 118.2, 119.4, 124.6, 129.3, 130.1, 132.1, 132.4, 157.6, 180.4.

Anal. calc. for $C_{12}H_8BrCl_2NO_2$: C, 41.30%; H, 2.31%; N, 4.01%. Found: C, 41.36%; H, 2.37%; N, 4.07%.

*4.1.2.8. (3-Bromo-4,5-dichloro-1H-pyrrol-2-yl)(5-bromo-2-methoxyphenyl)methanone (**13**).* This compound was obtained from reaction of **12** with equimolar amount of NBS, microwave heating at 90 °C, power of 60W for 4 cycles of 15 min each. White solid, Yield 89.1%, mp 185–186 °C. IR (cm^{-1}): 1611 (CO); 3207 (NH). ^{1}H NMR (DMSO-d_6) δ: 3.73 (s, 3H, CH_3), 7.10 (d, 1H, J = 8.9 Hz, H-3′), 7.46 (d, 1H, J = 2.5 Hz H-6′), 7.66 (dd, 1H, J = 8.9, 2.5 Hz, H-4'), 13.66 (bs, 1H, NH).

^{13}C NMR (DMSO-d_6) δ: 56.6, 107.4, 112.9, 114.6, 114.7, 125.5, 131.1, 133.0, 134.9, 141.0, 158.2, 180.3.

Anal. calc. for $C_{12}H_7Br_2Cl_2NO_2$: C, 33.68%; H, 1.65%; N, 3.27%. Found: C, 33.74%; H, 1.73%; N, 3.32%.

*4.1.2.9. General procedure for preparation of pyrrolomycins **1, 3, 4**.* In a typical experiment, to a solution of 1 mmol of **8,11,13** in 20 mL of anhydrous dichloromethane in an ice-salt bath, 4 g of $AlCl_3$ (30 mmol) was added. The reaction mixture was stirred overnight at room temperature. The solution was cautiously decomposed with ice-sulfuric acid 5% (30 mL), then 50 mL of diethyl ether was added. The mixture was stirred vigorously for 10 min, the organic layer was separated and the aqueous phase extracted with diethyl ether (2 × 30 mL). The combined extracts were washed with water until neutrality, dried over anhydrous sodium sulfate, and evaporated. The crude product was crystallized from dichloromethane to give pure pyrrolomycins **1,3,4**.

*(5-Bromo-2-hydroxyphenyl)(3,4,5-tribromo-1H-pyrrol-2-yl)methanone (**1**).* Yellow solid, Yield 63.1%, mp 193–194 °C. IR (cm^{-1}): 1615 (CO); 3253 (NH); 3322 (OH). ^{1}H NMR (DMSO-d_6) δ: 6.86 (d, 1H, J = 8.8 Hz, H-3′), 7.39 (s, 1H, H-6′), 7.48 (dd, 1H, J = 8.8, 2.6 Hz, H-4'), 10.24 (bs, 1H, OH), 13.47 (bs, 1H, NH). ^{13}C NMR (DMSO-d_6) δ: 104.8, 106.6, 110.4, 110.5, 119.1, 128.6, 131.2, 131.6, 134.9, 155.4, 182.1.

Anal. calc. for $C_{11}H_5Br_4NO_2$: C, 26.28%; H, 1.00%; N, 2.79%. Found: C, 26.33%; H, 1.05%; N, 2.84%.

*(5-bromo-2-hydroxyphenyl)(3,4-dibromo-5-chloro-1H-pyrrol-2-yl) methanone (**3**).* Yellow solid, Yield 68.7%, mp 190–191 °C. IR (cm^{-1}): 1621 (CO); 3247 (NH); 3361 (OH). ^{1}H NMR(DMSO-d_6) δ: 6.86 (d, 1H, J = 8.7 Hz, H-3′), 7.38 (s, 1H, H-6′), 7.48 (dd, 1H, J = 8.7, 2.6 Hz, H-4'), 10.24 (bs, 1H, OH), 13.47 (bs, 1H, NH). ^{13}C NMR (DMSO-d_6) δ: 104.8, 106.6, 110.4, 110.5, 119.1, 128.6, 131.2, 131.5, 134.9, 155.4, 182.1.

Anal. calc. for $C_{11}H_5Br_3ClNO_2$: C, 28.83%; H, 1.10%; N, 3.06%. Found: C, 28.87%; H, 1.16%; N, 3.12%.

*(3-Bromo-4,5-dichloro-1H-pyrrol-2-yl)(5-bromo-2-hydroxyphenyl) methanone (**4**).* Yellow solid, Yield 66.9%, mp 187–188 °C. IR (cm^{-1}): 1621 (CO); 3257 (NH); 3342 (OH). ^{1}H NMR (DMSO-d_6) δ: 6.87 (d, 1H, J = 8.7 Hz, H-3′), 7.39 (s, 1H, H-6′), 7.48 (dd, 1H, J = 8.7, 2.6 Hz, H-4'), 10.26 (bs, 1H, OH), 13.57 (bs, 1H, NH). ^{13}C NMR (DMSO-d_6) δ: 104.2, 110.4, 112.4, 119.0, 120.2, 128.2, 128.7, 131.5, 135.0, 155.4, 182.2.

Anal. calc. for $C_{11}H_5Br_2Cl_2NO_2$: C, 31.92%; H, 1.22%; N, 3.38%. Found: C, 31.99%; H, 1.26%; N, 3.42%.

4.2. Biology section

4.2.1. Cell cultures and treatments

The HCT116 colon cancer cell line, the MCF-7 breast cancer cell line, and the hTERT RPE-1 -immortalized retinal pigment epithelial cell line were obtained from American Type Culture Collection (ATCC, Manassas, VA, USA) and maintained in Dulbecco's Modified Eagle Medium

(DMEM) (Gibco, Paisley, UK), supplemented with 10% heat-inactivated fetal bovine serum and 100 U/mL penicillin and 100 μg/mL streptomycin, at 37 °C and 5% CO_2, as already described [49–52].

4.2.2. MTT viability assay

The cytotoxic activity of all chemically synthesized, namely PM **1–5**, was determined by using MTT assay [53,54]. After trypsinization, cells were plated at 5×10^3 cells/well in 96-well plates and incubated for 24 h before treatment. Stock solutions of DMSO dissolved- PMs (5 mM) were diluted to the desiderated concentrations (80 μM, 20 μM, 5 μM, 1.25 μM, 0.31 μM, 0.078 μM) in the culture medium, and added to the wells for further 48 h. After incubation, 20 μL of 5 mg mL-1of Thiazolyl Blue Tetrazolium Bromide (Merck, Darmstadt, Germany) in phosphate buffer saline (PBS) was added to each well in the dark and incubated for further 2 h at 37 °C.

After removing the medium containing MTT and washing it with PBS three times, 100 μL of DMSO was added to each well to dissolve formazan.

The absorbance was recorded at 570 nm using a 96-well plate reader (Spark® 20 M Tecan Trading AG, Switzerland). The percentage of cell viability compared to untreated control cells was calculated after subtraction of the blank. The IC_{50}, that is the concentration able to inhibit 50% of cell growth was calculated using a dose-response model, obtained from sigmoidal fitting of response curves of percent inhibition versus logarithmic concentration of PMs, using Graph Pad Prism software. Each result was the mean value of three different experiments performed in triplicate.

The selectivity index (SI) for HCT-116 and MCF-7 cells was calculated from the ratio of their IC_{50} values and that of the non-tumoral epithelial cell line h-TERT-RPE-1.

4.2.3. Clonogenicity assay

The HCT116 cells were seeded in a 24-well plate at a density of 5×10^4 cells/well. After 24 h, the cells were treated for 48 h with increased concentration of PMs (0.1–0.5 and 5 μM) and then incubated for another 7 days. The cells were fixed and stained with 6.0% (vol/vol) of glutaraldehyde and 0.5% (vol/vol) violet crystal solution for 30 min, washed several times to remove the excessive dye, and photographed. The crystal violet dye was dissolved by using a 5% (vol/vol) acetic acid solution and absorbance was recorded at 592 nm in the microplate reader.

4.2.4. Morphological assessment by phase contrast inverted microscope and Scanning Electron Microscopy (SEM)

Cells were seeded on a coverslip in 24-well plates at a density of 5×10^4 cells/well. After 24 h cells were treated for 48 h with appropriate concentrations of selected PMs. Morphology was observed under a phase contrast inverted microscope (Carl Zeiss, Oberkochen, Germany) at 200X.

For SEM analysis, the coverslips were extracted from the wells, rinsed with PBS pH 7.4, and fixed with glutaraldehyde 4% (vol/vol) at 4 °C for 30 min. After fixation, samples were washed several times with PBS and dehydrated with increasing ethanol solutions (15, 25, 50, 75, and 100% vol/vol). Finally, samples were dried, gold-sputtered, and observed with a SEM-FEI QUANTA 200F microscope (Thermo Fisher Scientific, MA USA). The SEM was set with an accelerated voltage equal to 10 kV.

4.2.5. Fluorescence staining with acridine orange/ethidium bromide (AO/EB), hoechst and rhodamine-phalloidin

Cells were seeded on a cover slip in 24-well plates at a density of 5×10^4 cells/well. After 24 h cells were treated for 48 h with appropriate concentrations of selected PMs. For AO/EB staining after incubation of selected PMs, coverslips were washed twice with PBS and stained for a few min with 200 μL of the Acridine Orange (100 μg/mL), Ethidium Bromide (100 μg/mL) mixture (1:1, v/v) and For Hoechst 33342 staining, coverslips were washed twice with PBS and stained for 10 min of Hoechst 33342, with a final concentration of 1 μg/ml. Cells were immediately observed under a fluorescent microscopy (Carl Zeiss, Oberkochen, Germany) at 640× magnification.

For Rhodamine-phalloidin staining coverslips were washed in PBS and cells were fixed in cold methanol for 15 min. After fixation, cells were permeabilized for 15 min in PBS- Triton X-100 0.1% (vol/vol). After washes with PBS cells were incubated with 0.165 μM of Rhodamine Phalloidin (Life Technology) for 40 min in the dark at room temperature. Cells were then washed with PBS and visualized at 640× magnification.

4.2.6. Western blotting

HCT116 cells seeded in dish plates were treated for 48 h h with 0.5 μM of selected PMs when reached 70% of confluence. After washing with PBS, cells were carefully scraped and incubated on ice for 30 min RIPA buffer. The total cellular lysate was centrifuged at 14,000 rpm for 10 min to clear cell debris and protein concentration determined by Bradford assay, as already reported [55–58]. Protein samples (20 μg/lane) were subjected to SDS polyacrylamide gel electrophoresis, then transferred to a nitrocellulose membrane (HyBond ECL, Amersham) and stained with Ponceau S (Sigma Aldrich Western blotting analysis was performed using a rabbit polyclonal antibodies for Akt 1-2-3, a goat polyclonal antibody for Beclin 1, a mouse monoclonal antibody for Actin-β (Santa Cruz, CA, USA), a rabbit polyclonal antibody for LC3 (Sigma Aldrich, Milano, Italia), a rabbit polyclonal antibodies for ATG7 and a mouse monoclonal for E-cadherin and vimentin (Cell Signaling Technology, Massachusetts, USA). Following incubation with the appropriate peroxidase-linked antibody, the reaction was revealed by the ECL detection system, using ChemiDoc™ MP System (Biorad, Milano, Italy) The correct protein loading was ascertained by immunoblotting for Actin-β. Bands quantification was performed by using Image J software.

4.2.7. Evaluation of ROS generation

Intracellular ROS levels were measured by using 2′,7′-dichlorodihydrofluorescein diacetate (DCFH-DA) HCT116 cells were plated in 96 well plates at a density of 5×10^3/well, allowed to grow overnight, and incubated for 24 h or 48 h with PMs-IC_{50} concentrations. At the end the medium was replaced with the culture medium containing DCFH-DA (10 μM) and incubated for 30 min at 37 °C. Then the medium was replaced with PBS and the fluorescence intensity was analysed by spectrofluorimeter with an excitation of 488 nm and emission wavelength of 525 nm. Data normalization was performed with parallel MTT assay. The experiments were performed in triplicate. Data are presented as average ± SD. For fluorescence microscopy analysis cells were seeded on a coverslip in 24 well plates at a density of 5×10^4 cells/well and treated in the same way.

Declaration of competing interest

The authors declare that they have no known competing financial interests or personal relationships that could have appeared to influence the work reported in this paper.

Data availability

Data will be made available on request.

Acknowledgments

This work was partially supported by grants from University of Palermo for M.V.R. (FFR-D15-160599) and P.C. (FFR-D15-160624). A special thanks to Professor Salvatore Petruso for His valuable advice and Dr. Giorgioo Nasillo of ATEN Center for SEM micrographs.

Appendix A. Supplementary data

Supplementary data to this article can be found online at https://doi.org/10.1016/j.ejmech.2023.115339.

References

[1] D.J. Newman, G.M. Cragg, Natural products as sources of new drugs from 1981 to 2014, J. Nat. Prod. 75 (2012) 311–335, https://doi.org/10.1021/np200906s.

[2] M.V. Raimondi, R. Listro, M.G. Cusimano, M. La Franca, T. Faddetta, G. Gallo, D. Schillaci, S. Collina, A. Leonchiks, G. Barone, Pyrrolomycins as antimicrobial agents. Microwave-assisted organic synthesis and insights into their antimicrobial mechanism of action, Bioorg. Med. Chem. 27 (2019) 721–728, https://doi.org/10.1016/j.bmc.2019.01.010.

[3] B. Maggio, D. Raffa, M.V. Raimondi, S. Cascioferro, F. Plescia, D. Schillaci, M. G. Cusimano, A. Leonchiks, D. Zhulenkovs, L. Basile, G. Daidone, Discovery of a new class of sortase a transpeptidase inhibitors to tackle gram-positive pathogens: 2-(2-phenylhydrazinylidene)alkanoic acids and related derivatives, Molecules 21 (2016) 241, https://doi.org/10.3390/molecules21020241.

[4] S. Cascioferro, B. Maggio, D. Raffa, M.V. Raimondi, M.G. Cusimano, D. Schillaci, B. Manachini, F. Plescia, G. Daidone, Synthesis and biofilm formation reduction of pyrazole-4-carboxamide derivatives in some Staphylococcus aureus strains, Eur. J. Med. Chem. 123 (2016) 58–68, https://doi.org/10.1016/j.ejmech.2016.07.030.

[5] K. Valderrama, E. Pradel, A.M. Firsov, H. Drobecq, H.B. le Roy, B. Villemagne, Y. N. Antonenko, R.C. Hartkoorn, Pyrrolomycins are potent natural protonophores, Antimicrob. Agents Chemother. 63 (2019), https://doi.org/10.1128/AAC.01450-19 e01450-19.

[6] M.V. Raimondi, A. Presentato, G. Li Petri, M. Buttacavoli, A. Ribaudo, V. De Caro, R. Alduina, P. Cancemi, New synthetic nitro-pyrrolomycins as promising antibacterial and anticancer agents, Antibiotics 9 (2020) 292, https://doi.org/10.3390/antibiotics9060292.

[7] T.R. McGuire, D.W. Coulter, D. Bai, J.A. Sughroue, J. Li, Z. Yang, Z. Qiao, Y. Liu, D. J. Murry, Y.S. Chhonker, E.M. McIntyre, G. Alexander, J.G. Sharp, R. Li, Effects of novel pyrrolomycin MP1 in MYCN amplified chemoresistant neuroblastoma cell lines alone and combined with temsirolimus, BMC Cancer 19 (2019) 837, https://doi.org/10.1186/s12885-019-6033-2.

[8] M. Barreca, V. Spanò, R. Rocca, R. Bivacqua, A.C. Abel, A. Maruca, A. Montalbano, M.V. Raimondi, C. Tarantelli, E. Gaudio, L. Cascione, A. Rinaldi, R. Bai, M. O. Steinmetz, A.E. Prota, S. Alcaro, E. Hamel, F. Bertoni, P. Barraja, Development of [1,2]oxazoloisoindoles tubulin polymerization inhibitors: further chemical modifications and potential therapeutic effects against lymphomas, Eur. J. Med. Chem. 243 (2022), 114744, https://doi.org/10.1016/j.ejmech.2022.114744.

[9] K. Grillone, C. Riillo, R. Rocca, S. Ascrizzi, V. Spanò, F. Scionti, N. Polerà, A. Maruca, M. Barreca, G. Juli, M. Arbitrio, M.T. Di Martino, D. Caracciolo, P. Tagliaferri, S. Alcaro, A. Montalbano, P. Barraja, P. Tassone, The new microtubule-targeting agent SIX2G induces immunogenic cell death in multiple myeloma, Int. J. Mol. Sci. 23 (2022) 1–16, https://doi.org/10.3390/ijms231810222.

[10] M. Labbozzetta, M. Barreca, V. Spanò, M.V. Raimondi, P. Poma, M. Notarbartolo, P. Barraja, A. Montalbano, Novel insights on [1,2]oxazolo[5,4-e]isoindoles on multidrug resistant acute myeloid leukemia cell line, Drug Dev. Res. 83 (2022) 1331–1341, https://doi.org/10.1002/ddr.21962.

[11] M. Barreca, A.M. Ingarra, M.V. Raimondi, V. Spanò, M. De Franco, L. Menilli, V. Gandin, G. Miolo, P. Barraja, A. Montalbano, Insight on pyrimido[5,4-g] indolizine and pyrimido[4,5-c]pyrrolo[1,2-a]azepine systems as promising photosensitizers on malignant cells, Eur. J. Med. Chem. 237 (2022), 114399, https://doi.org/10.1016/j.ejmech.2022.114399.

[12] M. Barreca, A.M. Ingarra, M.V. Raimondi, V. Spanò, A.P. Piccionello, M. De Franco, L. Menilli, V. Gandin, G. Miolo, P. Barraja, A. Montalbano, New tricyclic systems as photosensitizers towards triple negative breast cancer cells, Arch Pharm. Res. (Seoul) 45 (2022) 806–821, https://doi.org/10.1007/s12272-022-01414-1.

[13] V. Spanò, M. Barreca, V. Cilibrasi, M. Genovese, M. Renda, A. Montalbano, L.J. V. Galietta, P. Barraja, Evaluation of fused pyrrolothiazole systems as correctors of mutant CFTR protein, Molecules 26 (2021) 1–25, https://doi.org/10.3390/molecules26051275.

[14] B. Maggio, M.V. Raimondi, D. Raffa, F. Plescia, S. Cascioferro, G. Cancemi, M. Tolomeo, S. Grimaudo, G. Daidone, Synthesis and antiproliferative activity of 3-(2-chloroethyl)-5-methyl-6-phenyl-8-(trifluoromethyl)-5,6-dihydropyrazolo[3,4-*f*][1,2,3,5]tetrazepin-4-(3H)-one, Eur. J. Med. Chem. 96 (2015) 98–104, https://doi.org/10.1016/j.ejmech.2015.04.004.

[15] B. Maggio, M.V. Raimondi, D. Raffa, F. Plescia, S. Cascioferro, S. Plescia, M. Tolomeo, A. Di Cristina, R.M. Pipitone, S. Grimaudo, G. Daidone, Synthesis of substituted 3-amino-N-phenyl-1H-indazole-1-carboxamides endowed with antiproliferative activity, Eur. J. Med. Chem. 46 (2011) 168–174, https://doi.org/10.1016/j.ejmech.2010.10.032.

[16] N. Ezaki, M. Koyama, T. Shomura, T. Tsuruoka, S. Inouye, Pyrrolomyclns C, D and E, new members of pyrrolomycins, J. Antibiot. (Tokyo) 36 (1983) 1263–1267, https://doi.org/10.7164/antibiotics.36.1263.

[17] N. Ezaki, M. Koyama, Y. Kodama, T. Shomura, K. Tashiro, T. Tsuruoka, S. Inouye, Pyrrolomycins F1 F2a, F2b and F3, new metabolites produced by the addition of bromide to the fermentation, J. Antibiot. (Tokyo) 36 (1983) 1431–1438, https://doi.org/10.7164/antibiotics.36.1431.

[18] P. Hodge, R.W. Rickards, The halogenation of methyl pyrrole-2-carboxylate and of some related pyrroles, J. Chem. Soc. 11 (1965) 459–470, https://doi.org/10.1039/JR9650000459.

[19] P. Cancemi, M. Buttacavoli, F. D'Anna, S. Feo, R.M. Fontana, R. Noto, A. Sutera, P. Vitale, G. Gallo, The effects of structural changes on the anti-microbial and anti-proliferative activities of diimidazolium salts, New J. Chem. 41 (2017) 3574–3585, https://doi.org/10.1039/c6nj03904a.

[20] H. Kyykallio, S. Oikari, M.B. Álvez, C.J.G. Dodd, J. Capra, K. Rilla, The density and length of filopodia associate with the activity of hyaluronan synthesis in tumor cells, Cancers 12 (2020) 1908, https://doi.org/10.3390/cancers12071908.

[21] P.K. Mattila, P. Lappalainen, Filopodia: molecular architecture and cellular functions, Nat. Rev. Mol. Cell Biol. 9 (2008) 446–454, https://doi.org/10.1038/nrm2406.

[22] J. Swanson, C. Watts, Macropinocytosis, Trends Cell Biol. 5 (1995) 424–428, https://doi.org/10.1016/s0962-8924(00)89101-1.

[23] H. Bierne, E. Gouin, P. Roux, P. Caroni, H.L. Yin, P. Cossart, A role for cofilin and LIM kinase in Listeria-induced phagocytosis, J. Cell Biol. 155 (2001) 101–112, https://doi.org/10.1083/jcb.200104037.

[24] J. Bi, R. Wang, X. Zeng, Lipid rafts regulate the lamellipodia formation of melanoma A375 cells via actin cytoskeleton-mediated recruitment of β1 and β3 integrin, Oncol. Lett. 16 (2018) 6540–6546, https://doi.org/10.3892/ol.2018.9466.

[25] H.F.G. Heijnen, M. Van Lier, S. Waaijenborg, Y. Ohno-Iwashita, A.A. Waheed, M. Inomata, G. Gorter, W. Möbius, J.W.N. Akkerman, J.W. Slot, Concentration of rafts in platelet filopodia correlates with recruitment of c-Src and CD63 to these domains, J. Thromb. Haemostasis 1 (2003) 1161–1173, https://doi.org/10.1046/j.1538-7836.2003.00316.x.

[26] A.V. Shubin, I.V. Demidyuk, A.A. Komissarov, L.M. Rafieva, S.V. Kostrov, Cytoplasmic vacuolization in cell death and survival, Oncotarget 7 (2016) 55863–55889, https://doi.org/10.18632/oncotarget.10150.

[27] T. Aki, A. Nara, K. Uemura, Cytoplasmic vacuolization during exposure to drugs and other substances, Cell Biol. Toxicol. 28 (2012) 125–131, https://doi.org/10.1007/s10565-012-9212-3.

[28] W.A. Maltese, J.H. Overmeyer, Methuosis: nonapoptotic cell death associated with vacuolization of macropinosome and endosome compartments, Am. J. Pathol. 184 (2014) 1630–1642, https://doi.org/10.1016/j.ajpath.2014.02.028.

[29] J.W. Ady, S. Desir, V. Thayanithy, R.I. Vogel, A.L. Moreira, R.J. Downey, Y. Fong, K. Manova-Todorova, M.A.S. Moore, E. Lou, Intercellular communication in malignant pleural mesothelioma: properties of tunneling nanotubes, Front. Physiol. 5 (2014) 1–16, https://doi.org/10.3389/fphys.2014.00400.

[30] H.H. Gerdes, A. Rustom, X. Wang, Tunneling nanotubes, an emerging intercellular communication route in development, Mech. Dev. 130 (2013) 381–387, https://doi.org/10.1016/j.mod.2012.11.006.

[31] A. Rustom, R. Saffrich, I. Markovic, P. Walther, H.H. Gerdes, Nanotubular highways for intercellular organelle transport, Science 303 (2004) 1007–1010, https://doi.org/10.1126/science.1093133.

[32] S. Abounit, C. Zurzolo, Wiring through tunneling nanotubes - from electrical signals to organelle transfer, J. Cell Sci. 125 (2012) 1089–1098, https://doi.org/10.1242/jcs.083279.

[33] A. Raghavan, P. Rao, J. Neuzil, D.L. Pountney, S. Nath, Oxidative stress and Rho GTPases in the biogenesis of tunnelling nanotubes: implications in disease and therapy, Cell. Mol. Life Sci. 79 (2022) 36, https://doi.org/10.1007/s00018-021-04040-0.

[34] J.L. Spees, S.D. Olson, M.J. Whitney, D.J. Prockop, Mitochondrial transfer between cells can rescue aerobic respiration, Proc. Natl. Acad. Sci. U. S. A 103 (2006) 1283–1288, https://doi.org/10.1073/pnas.0510511103.

[35] M. Buttacavoli, N.N. Albanese, G. Di Cara, R. Alduina, C. Faleri, M. Gallo, G. Pizzolanti, G. Gallo, S. Feo, F. Baldi, P. Cancemi, Anticancer activity of biogenerated silver nanoparticles: an integrated proteomic investigation, Oncotarget 9 (2018) 9685–9705, https://doi.org/10.18632/oncotarget.23859.

[36] J. Lertsuwan, K. Lertsuwan, A. Sawasdichai, N. Tasnawijitwong, K.Y. Lee, P. Kitchen, S. Afford, K. Gaston, P.S. Jayaraman, J. Satayavivad, CX-4945 induces methuosis in cholangiocarcinoma cell lines by a CK2-independent mechanism, Cancers 10 (2018) 283, https://doi.org/10.3390/cancers10090283.

[37] L. Galluzzi, I. Vitale, J.M. Abrams, E.S. Alnemri, E.H. Baehrecke, M. V. Blagosklonny, T.M. Dawson, V.L. Dawson, W.S. El-Deiry, S. Fulda, E. Gottlieb, D. R. Green, M.O. Hengartner, O. Kepp, R.A. Knight, S. Kumar, S.A. Lipton, X. Lu, F. Madeo, W. Malorni, P. Mehlen, G. Nūez, M.E. Peter, M. Piacentini, D. C. Rubinsztein, Y. Shi, H.U. Simon, P. Vandenabeele, E. White, J. Yuan, B. Zhivotovsky, G. Melino, G. Kroemer, Molecular definitions of cell death subroutines: recommendations of the nomenclature committee on cell death 2012, Cell Death Differ. 19 (2012) 107–120, https://doi.org/10.1038/cdd.2011.96.

[38] P. Weerasinghe, L.M. Buja, Oncosis, An important non-apoptotic mode of cell death, Exp. Mol. Pathol. 93 (2012) 302–308, https://doi.org/10.1016/j.yexmp.2012.09.018.

[39] R.K. Hylton, J.E. Heebner, M.A. Grillo, M.T. Swulius, Cofilactin filaments regulate filopodial structure and dynamics in neuronal growth cones, Nat. Commun. 13 (2022) 1–11, https://doi.org/10.1038/s41467-022-30116-x.

[40] R.K. Hylton, J.E. Heebner, M.A. Grillo, M.T. Swulius, Cofilactin filaments regulate filopodial structure and dinamics in neuronal growth cones, Nat. Commun. 13 (2022) 2439, https://doi.org/10.1038/s41467-022-30116-x.

[41] Q. Xu, L.P. Huff, M. Fujii, K.K. Griendling, Redox regulation of the actin cytoskeleton and its role in the vascular system, Free Radic. Biol. Med. 109 (2017) 84–107, https://doi.org/10.1016/j.freeradbiomed.2017.03.004.

[42] D. Zhu, K.S. Tan, X. Zhang, A.Y. Sun, G.Y. Sun, J.C.M. Lee, Hydrogen peroxide alters membrane and cytoskeleton properties and increases intercellular

connections in astrocytes, J. Cell Sci. 118 (2005) 3695–3703, https://doi.org/10.1242/jcs.02507.
[43] M. Schieber, N.S. Chandel, ROS function in redox signaling, Curr. Biol. 24 (2014) 453–462, https://doi.org/10.1016/j.cub.2014.03.034.ROS.
[44] W. Ornatowski, Q. Lu, M. Yegambaram, A.E. Garcia, E.A. Zemskov, E. Maltepe, J. R. Fineman, T. Wang, S.M. Black, Complex interplay between autophagy and oxidative stress in the development of pulmonary disease, Redox Biol. 36 (2020), 101679, https://doi.org/10.1016/j.redox.2020.101679.
[45] E.L. Thomas, Myeloperoxidase-hydrogen peroxide-chloride antimicrobial system: effect of exogenous amines on antibacterial action against Escherichia coli, Infect. Immun. 25 (1979) 110–116, https://doi.org/10.1128/iai.25.1.110-116.1979.
[46] W. Gottardi, M. Nagl, N-chlorotaurine, a natural antiseptic with outstanding tolerability, J. Antimicrob. Chemother. 65 (2010) 399–409, https://doi.org/10.1093/jac/dkp466.
[47] C.L. Hawkins, B.E. Brown, M.J. Davies, Hypochlorite-and hypobromite-mediated radical formation and its role in cell lysis, Arch. Biochem. Biophys. 395 (2001) 137–145, https://doi.org/10.1006/abbi.2001.2581.
[48] W. Gottardi, S. Klotz, M. Nagl, Superior bactericidal activity of N-bromine compounds compared to their N-chlorine analogues can be reversed under protein load, J. Appl. Microbiol. 116 (2014) 1427–1437, https://doi.org/10.1111/jam.12474.
[49] I. Pucci-Minafra, N. Albanese, G. Di Cara, L. Minafra, M.R. Marabeti, P. Cancemi, Breast cancer cells exhibit selective modulation induced by different collagen substrates, Connect. Tissue Res. 49 (2008) 252–256, https://doi.org/10.1080/03008200802147779.
[50] A. Coppola, L. Tomasello, G. Pizzolanti, I. Pucci-Minafra, N. Albanese, G. Di Cara, P. Cancemi, M. Pitrone, A. Bommarito, E. Carissimi, G. Zito, A. Criscimanna, A. Galluzzo, C. Giordano, In vitro phenotypic, genomic and proteomic characterization of a cytokine-resistant murine β-TC3 cell line, PLoS One 7 (2012), e32109, https://doi.org/10.1371/journal.pone.0032109.
[51] I. Pucci-Minafra, P. Cancemi, G. Di Cara, L. Minafra, S. Feo, A. Forlino, M.E. Tira, R. Tenni, D. Martini, A. Ruggeri, S. Minafra, Decorin transfection induces proteomic and phenotypic modulation in breast cancer cells 8701-BC, Connect, Tissue Res 49 (2008) 30–41, https://doi.org/10.1080/03008200701820443.
[52] M.L. Saladino, M. Markowska, C. Carmone, P. Cancemi, R. Alduina, A. Presentato, R. Scaffaro, D. Biały, M. Hasiak, D. Hreniak, M. Wawrzyńska, Graphene oxide carboxymethylcellulose nanocomposite for dressing materials, Materials 13 (2020) 1–14, https://doi.org/10.3390/MA13081980.
[53] M. Massaro, G. Barone, V. Barra, P. Cancemi, A. Di Leonardo, G. Grossi, F. Lo Celso, S. Schenone, C. Viseras Iborra, S. Riela, Pyrazole[3,4-d]pyrimidine derivatives loaded into halloysite as potential CDK inhibitors, Int. J. Pharm. 599 (2021), 120281, https://doi.org/10.1016/j.ijpharm.2021.120281.
[54] C. Rizzo, P. Cancemi, L. Mattiello, S. Marullo, F. D'Anna, Naphthalimide imidazolium-based supramolecular hydrogels as bioimaging and theranostic soft materials, ACS Appl. Mater. Interfaces 12 (2020) 48442–48457, https://doi.org/10.1021/acsami.0c17149.
[55] P. Cancemi, G. Di Cara, N.N. Albanese, F. Costantini, M.R. Marabeti, R. Musso, I. Riili, C. Lupo, E. Roz, I. Pucci-Minafra, Differential occurrence of S100A7 in breast cancer tissues: a proteomic-based investigation, Proteomics -, Clin. Appl. 6 (2012) 364–373, https://doi.org/10.1002/prca.201100072.
[56] I. Caon, M.L. D'angelo, B. Bartolini, E. Caravà, A. Parnigoni, F. Contino, P. Cancemi, P. Moretto, N.K. Karamanos, A. Passi, D. Vigetti, E. Karousou, M. Viola, The secreted protein c10orf118 is a new regulator of hyaluronan synthesis involved in tumour-stroma cross-talk, Cancers 13 (2021) 1105, https://doi.org/10.3390/cancers13051105.
[57] M. Buttacavoli, N.N. Albanese, E. Roz, I. Pucci-Minafra, S. Feo, P. Cancemi, Proteomic profiling of colon cancer tissues: Discovery of new candidate biomarkers, Int. J. Mol. Sci. 21 (2020) 3096, https://doi.org/10.3390/ijms21093096.
[58] R. Melfi, P. Cancemi, R. Chiavetta, V. Barra, L. Lentini, A. Di Leonardo, Investigating REPAIRv2 as a tool to edit CFTR mRNA with premature stop codons, Int. J. Mol. Sci. 21 (2020) 4781, https://doi.org/10.3390/ijms21134781.